






# The age–chemical abundance structure of the Galaxy I: evidence for a late-accretion event in the outer disc at $z \sim 0.6$

Jianhui Lian <sup>1</sup>★, Daniel Thomas <sup>1</sup>, Claudia Maraston,<sup>1</sup> Olga Zamora,<sup>2,3</sup> Jamie Tayar <sup>4</sup>, Kaike Pan,<sup>5</sup> Patricia Tissera <sup>6</sup>, José G. Fernández-Trincado <sup>7</sup> and D. A. Garcia-Hernandez<sup>2,3</sup>

<sup>1</sup>*Institute of Cosmology and Gravitation, University of Portsmouth, Burnaby Road, Portsmouth PO1 3FX, UK*

<sup>2</sup>*Instituto de Astrofísica de Canarias, E-38205 La Laguna, Tenerife, Spain*

<sup>3</sup>*Departamento de Astrofísica, Universidad de La Laguna (ULL), E-38206 La Laguna, Tenerife, Spain*

<sup>4</sup>*Institute for Astronomy, University of Hawaii, 2680 Woodlawn Drive, Honolulu, HI 96822, USA*

<sup>5</sup>*Apache Point Observatory, PO Box 59, Sunspot, NM 88349, USA*

<sup>6</sup>*Departamento de Ciencias Físicas, Universidad Andres Bello, 700 Fernandez Concha, Santiago, Chile*

<sup>7</sup>*Instituto de Astronomía y Ciencias Planetarias, Universidad de Atacama, Copayapu 485, Copiapó, Chile*

Accepted 2020 March 25. Received 2020 March 23; in original form 2019 August 8

## ABSTRACT

We investigate the age–chemical abundance structure of the outer Galactic disc at a galactocentric distance of  $r > 10$  kpc as recently revealed by the SDSS/APOGEE survey. Two sequences are present in the  $[\alpha/\text{Fe}]$ – $[\text{Fe}/\text{H}]$  plane with systematically different stellar ages. Surprisingly, the young sequence is less metal rich, suggesting a recent dilution process by additional gas accretion. As the stars with the lowest iron abundance in the younger sequence also show an enhancement in  $\alpha$ -element abundance, the gas accretion event must have involved a burst of star formation. In order to explain these observations, we construct a chemical evolution model. In this model, we include a relatively short episode of gas accretion at late times on top of an underlying secular accretion over long time-scales. Our model is successful at reproducing the observed distribution of stars in the three-dimensional space of  $[\alpha/\text{Fe}]$ – $[\text{Fe}/\text{H}]$ –age in the outer disc. We find that a late-time accretion with a delay of 8.2 Gyr and a time-scale of 0.7 Gyr best fits the observed data, in particular the presence of the young, metal-poor sequence. Our best-fitting model further implies that the amount of accreted gas in the late-time accretion event needs to be about three times the local gas reservoir in the outer disc at the time of accretion in order to sufficiently dilute the metal abundance. Given this large fraction, we interpret the late-time accretion event as a minor merger presumably with a gas-rich dwarf galaxy with a mass  $M_* < 10^9 M_\odot$  and a gas fraction of  $\sim 75$  per cent.

**Key words:** Galaxy: abundances – Galaxy: disc – Galaxy: evolution – Galaxy: formation – Galaxy: stellar content.

## 1 INTRODUCTION

Stars serve as a fossil record in galaxies carrying key information about a galaxy’s formation history. In particular, the chemical abundances of stars are like footprints of the interstellar material from which the stars were formed. The interstellar medium (ISM) in a galaxy is enriched with chemical elements through the cycle of stars forming, evolving, and dying. Therefore, the investigation of the chemical composition of stars and stellar populations is a powerful tool to unfold the chemical enrichment and formation

history of a galaxy. The Milky Way (MW) provides an ideal laboratory to study galactic chemical evolution and test galaxy formation and evolution models because of our ability to resolve stellar populations into individual stars and to measure detailed chemical element abundances.

The abundances of iron (Fe) and the  $\alpha$ -elements (e.g. Mg, O, Ca, etc.) are of particular interest and widely used to constrain the chemical evolution of our Galaxy. The distribution of iron abundance, i.e. the metallicity distribution function (MDF), has been used to constrain chemical evolution models for a long time (e.g. Schmidt 1963; Pagel & Patchett 1975) and more recently also in a cosmological framework (Tumlinson 2010). It was shown early on that the observed MDF in the solar neighbourhood disfavors a

\* E-mail: [u6016389@utah.edu](mailto:u6016389@utah.edu)

closed-box model (van den Bergh 1962; Pagel & Patchett 1975), as the latter overestimates the density of metal-poor stars ( $[\text{Fe}/\text{H}] < -0.2$  dex). A leaky/accretion model including gas inflow and/or outflow is one of the preferred solutions to this problem (e.g. Audouze & Tinsley 1976; Pagel 1997). The observed abundance of  $\alpha$ -elements combined with Fe further constrains the time-scale of star formation. This is because  $\alpha$ -elements are released promptly through SN-II explosions of massive stars (with a time delay of only a few 10 Myr) while the enrichment of Fe is dominated by SN-Ia explosions of long-lived, low-mass stars (with longer delay times from a few 10 Myr to a few 10 Gyr). Hence, a low ratio of  $[\alpha/\text{Fe}]$  indicates a long period of star formation, while a high  $[\alpha/\text{Fe}]$  suggests that star formation must have occurred on short time-scales such that SN-Ia did not have the time to release iron (Matteucci 1994). This powerful diagnostic has been extended to galaxies, demonstrating that the most massive galaxies formed their stars on the shortest time-scales due to their enhanced  $[\alpha/\text{Fe}]$  ratios (Thomas et al. 2010).

One of the most interesting discoveries regarding the chemical compositions of stars in the MW is the bimodal distribution in the  $[\alpha/\text{Fe}]$ – $[\text{Fe}/\text{H}]$  plane in which most stars lie on two well-separated sequences (Fuhrmann 1998; Reddy, Lambert & Allende Prieto 2006; Adibekyan et al. 2012; Haywood et al. 2013; Bensby, Feltzing & Oey 2014). One sequence comprises stars with supersolar  $\alpha$ -abundance ( $[\alpha/\text{Fe}] > 0.15$ ) while the other consists of stars with solar-like abundance ratios ( $[\alpha/\text{Fe}] \sim 0$ ). The high- $\alpha$  sequence is generally more metal poor than the low- $\alpha$  sequence, but both of them span a wide range in metallicity. There is a significant overlap in metallicity between the two sequences. This pattern was first identified for the solar neighbourhood and then recently confirmed to be valid for a large portion of the MW disc (Hayden et al. 2015).

Besides chemical composition, age is a further fundamental stellar parameter providing deep insight into the Galaxy’s formation history. Combining the observed ages and chemical compositions of stars in the MW allows us to unfold the chemical enrichment history in great detail. However, stellar age measurements are challenging. One way to obtain stellar ages is to match well-determined stellar parameters  $T_{\text{eff}}$ ,  $\log g$ , and  $[\text{Fe}/\text{H}]$  to the isochrones of stellar evolution models (e.g. Jørgensen & Lindegren 2005). An alternative method combines asteroseismology and spectroscopic observations to set constraints on the stellar mass and then derive the stellar age (e.g. Pinsonneault et al. 2014). Both these methods require high-quality spectroscopy.

For a long time, spectroscopic observations were limited to the stars in the solar vicinity (e.g. Haywood et al. 2013; Bergemann et al. 2014). A number of recent, large spectroscopic surveys such as SDSS/APOGEE (Majewski et al. 2017), LAMOST (Zhao et al. 2012), and GALAH (De Silva et al. 2015) have improved the situation significantly, providing high-quality optical/infrared spectra with well-determined element abundances and other stellar properties for  $\sim 10^5$  stars across the Galactic disc. With these large spectroscopic surveys, it is now possible to map the age–chemical abundance structure of the Galactic disc well beyond the solar radius. For example, Ness et al. (2016) derive the ages of 70 000 stars from high-quality APOGEE spectra. The authors apply a machine learning algorithm to estimate the stellar mass from the high-resolution spectra and to then infer the age. A group of stars with more reliable masses from asteroseismology observations (Pinsonneault et al. 2014) are used as a training set. A similar approach is used by Wu et al. (2019) to derive the masses and ages for stars observed by the LAMOST survey.

In this new era of large spectroscopic surveys reaching well beyond the solar neighbourhood, theoretical models that are capable to explain the new data are needed to improve our understanding of MW formation and evolution. We therefore started a campaign in which we use our chemical evolution model (Lian et al. 2018a) to analyse the large sample of stars with age and chemical composition measurements from the APOGEE survey. Our ultimate goal is to shed light on the physical mechanisms responsible for the bimodality in the  $[\alpha/\text{Fe}]$ – $[\text{Fe}/\text{H}]$  plane and the formation of the two separate populations in the Galactic disc. Given the complexity of the topic, we present this work in separate papers. In this first paper, we focus on the combined age–chemical abundance structure of the *outer* Galactic disc at  $r > 10$  kpc. The next paper of this series will focus on the combined age–chemical abundance structure of the inner disc and the bulge.

In this paper, we propose a new outer disc formation scenario in which a late-time gas accretion event is invoked to explain the coexistence of old metal-rich and young metal-poor stars in the outer disc. A similar idea of delayed gas accretion was proposed recently in chemical evolution models (Noguchi 2018; Haywood et al. 2019; Spitoni et al. 2019) to explain the  $[\alpha/\text{Fe}]$ – $[\text{Fe}/\text{H}]$  distribution in the solar neighbourhood. A similar scenario was previously presented in the semi-analytical model by Calura & Menci (2009). This scenario gets further support from recent cosmological simulations reporting the existence of a bimodality in the  $[\alpha/\text{Fe}]$ – $[\text{Fe}/\text{H}]$  sequence caused by the occurrence of two phases of disc formation through gas accretion (Grand et al. 2017; Mackereth et al. 2018; Clarke et al. 2019). Here we use a chemical evolution model to provide further constraints on a possible late accretion phase based on the age–chemical abundance structure of the outer disc. Our analysis goes beyond the solar neighbourhood providing evidence of an accretion event affecting the disc at radii at least up to two times the solar radius.

The structure of this paper is organized as follows. We introduce the sample selection and observational results in Section 2. A general introduction of our chemical evolution model is presented in Section 3. A direct comparison between models and observations with an illustration of our best-fitting model is included in Section 4. We then discuss the implications of the results in Section 5 and conclude with Section 6.

## 2 DATA

The sample analysed here comprises red clump and red giant stars that were observed by the Apache Point Observatory Galactic Evolution Experiment (APOGEE) survey (Majewski et al. 2017), which is part of the Sloan Digital Sky Survey (SDSS; Blanton et al. 2017). APOGEE targets primarily horizontal branch and red giant branch stars throughout the MW’s bulge, disc, and halo (Zasowski et al. 2013, 2017), using the 2.5 m Sloan Telescope at Apache Point Observatory (Gunn et al. 2006) and the 2.5 m du Pont telescope at Las Campanas Observatory. Both telescopes are equipped with high-resolution,  $H$ -band spectrographs (Wilson et al. 2012, 2019). Data are reduced and stellar velocities, parameters, and abundances are determined using custom pipelines described in Nidever et al. (2015) and García Pérez et al. (2016). Here, we use stellar metallicities,  $\alpha$ -element abundances, and stellar ages from Ness et al. (2016), which are based on spectra and pipeline parameters released as part of SDSS/APOGEE Data Release 12 (DR12; Alam et al. 2015; Holtzman et al. 2015). Stellar coordinates are taken from APOGEE’s DR14 catalogue (Abolfathi et al. 2018; Holtzman et al. 2018), and we use the ‘NMSU’ stellar distances in

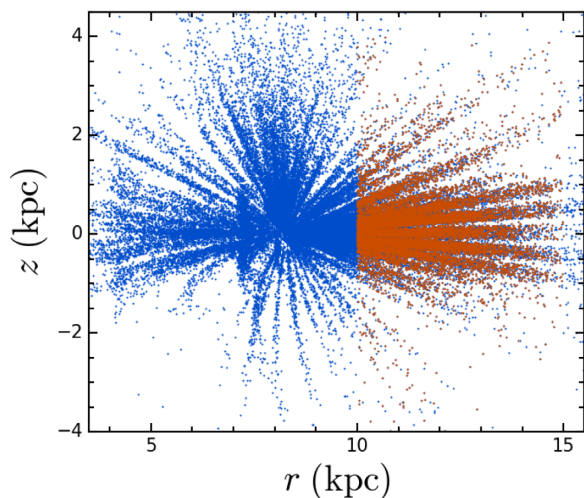


**Figure 1.** Spatial distribution of stars in the parent sample (blue dots) and our target sample in the outer disc with  $r > 10$  kpc and  $S/N > 60$  (brown dots). The  $x$ -axis indicates the cylindrical radial Galactocentric distance, and the  $y$ -axis is the vertical distance from the Galactic mid-plane.

the APOGEE DR14 distances Value Added Catalogue.<sup>1</sup> We verified that our results do not depend significantly on the choice of set of stellar distances.

## 2.1 Sample selection

To ensure a high quality of stellar parameter measurements, we use an additional cut in signal-to-noise (SNR), selecting stars from the parent sample with SNR above 60. We further exclude stars with low-quality spectra as indicated by the flags BAD and WARN in the APOGEE catalogue. We also exclude stars with unreliable parameter estimates selecting stars with  $\text{flag}_{[\alpha/\text{Fe}]} = 0$  and  $\text{flag}_{[\text{Fe}/\text{H}]} = 0$  in the star-level bitmask.

Fig. 1 shows the spatial distribution of the stars in the parent sample (blue dots) in the  $r$ - $z$  plane. The  $x$ -axis indicates the cylindrical radial Galactocentric distance, and the  $y$ -axis is the vertical distance from the Galactic mid-plane. In this paper, we focus on the *outer* disc with  $10 < r < 15$  kpc. The brown dots indicate the spatial distribution of the final selected sample.

We know from observations of the solar neighbourhood that the disc of the MW contains two distinct stellar populations: an old population with high  $[\alpha/\text{Fe}]$  ratios and a young/intermediate-age population with low  $[\alpha/\text{Fe}]$  ratios (e.g. Fuhrmann 1998). Recent large spectroscopic surveys of the stars in the MW (e.g. Adibekyan et al. 2011; Hayden et al. 2015) have revealed that there is a clear bimodal distribution of disc stars in the  $[\alpha/\text{Fe}]$ - $[\text{Fe}/\text{H}]$  plane as shown in Fig. 2. The left-hand panel shows the distribution for the entire disc, while the middle and right-hand panels are for the inner ( $4 < r < 8$  kpc) and outer ( $10 < r < 15$  kpc) discs, respectively. It can be seen that a clear bimodality in the distribution is present in the inner disc but it disappears in the outer disc.

These two distinct stellar populations are usually referred to as the chemical thick and thin discs. The chemical thick disc is represented by the high- $\alpha$  branch while the chemical thin disc is composed of the low- $\alpha$  branch. To separate the two populations, Adibekyan et al.

(2011) proposed an empirical solution that is based on the minimum number density between the two branches. A similar form of the separation but based on visual inspection of our sample is shown as the dashed black lines in Fig. 2.

In the inner disc, a significant fraction of both low- and high- $\alpha$  populations coexist while the outer disc is clearly dominated by the low- $\alpha$  population. This suggests that the formation of the low- $\alpha$  population in the disc is physically decoupled from the high- $\alpha$  population. In this work, we focus on the Galactic outer disc ( $10 < r < 15$  kpc) and on the formation of the low- $\alpha$  population. The final sample contains 15 722 disc stars shown in the right-hand panel of Fig. 2.

## 2.2 Element abundance and age determination

The element abundance and age measurements are adopted from Ness et al. (2016). State-of-the-art stellar ages come from asteroseismology observations that provide information about stellar interiors and hence their masses. The stellar mass then sets strong constraints on the stellar age for post-main-sequence stars (Martig et al. 2015). The fractional uncertainty in the age derived in this way can be as low as  $\sim 20$  per cent (i.e. the  $1\sigma$  scatter at the age of 5 Gyr is 1 Gyr, for example).

Asteroseismology surveys in the literature generally only cover a relatively small portion of the Galaxy (Borucki et al. 2010). Moreover, due to the distance limitation in the asteroseismology data, the stellar sample with accurate seismic ages is usually restricted to relatively nearby stars in the solar neighbourhood. The currently largest stellar sample with seismic ages is the APOKASC catalogue (Pinsonneault et al. 2018) based on the Kepler and APOGEE data. The latest version of the APOKASC catalogue contains 5442 stars.

Given these limitations, Ness et al. (2016) developed a data-driven link between the asteroseismic data for nearby stars and the spectroscopic data for distant stars based on a machine learning algorithm. This calibration allowed them to determine chemical abundances ( $[\text{Fe}/\text{H}]$  and  $[\alpha/\text{Fe}]$ ), masses, and ages of giant stars directly from spectra. An early version of the APOKASC catalogue (Pinsonneault et al. 2014) containing 1639 stars with spectroscopic measurements ( $T_{\text{eff}}$ ,  $[\alpha/\text{Fe}]$ ,  $[\text{Fe}/\text{H}]$ ) from APOGEE DR12 (Holtzman et al. 2015) and seismic measurements (stellar mass,  $\log g$ ) from Kepler was used as a training sample. Stellar ages were then derived by matching these stellar parameters to PARSEC isochrones (Bressan et al. 2012). Based on this training set, Ness et al. (2016) estimated the ages of 70 000 APOGEE stars from APOGEE spectra. The typical uncertainty of the ages is 40 per cent, hence 0.2 dex.

### 2.2.1 Assessment of the Ness et al. ages

We perform an additional test in order to check the reliability of the spectroscopic ages used here. As already mentioned, the ages are calibrated to the seismic ages from the older version of APOKASC with 1639 stars. With updated Kepler observations, the latest version of the APOKASC catalogue has now been expanded to 5442 stars. Therefore, we can directly assess the quality of these ages by comparing them with the new seismic ages of those 3803 stars that were not included in the original training set.

The comparison is shown in Fig. 3. The dashed line indicates the one-to-one relation. It can be seen that the ages from these two measurements are well correlated with a Pearson’s correlation coefficient of 0.69. The scatter of the correlation is 0.26 dex on

<sup>1</sup>[https://www.sdss.org/dr14/data\\_access/value-added-catalogs/?vac.id=apogee-dr14-based-distance-estimations](https://www.sdss.org/dr14/data_access/value-added-catalogs/?vac.id=apogee-dr14-based-distance-estimations)

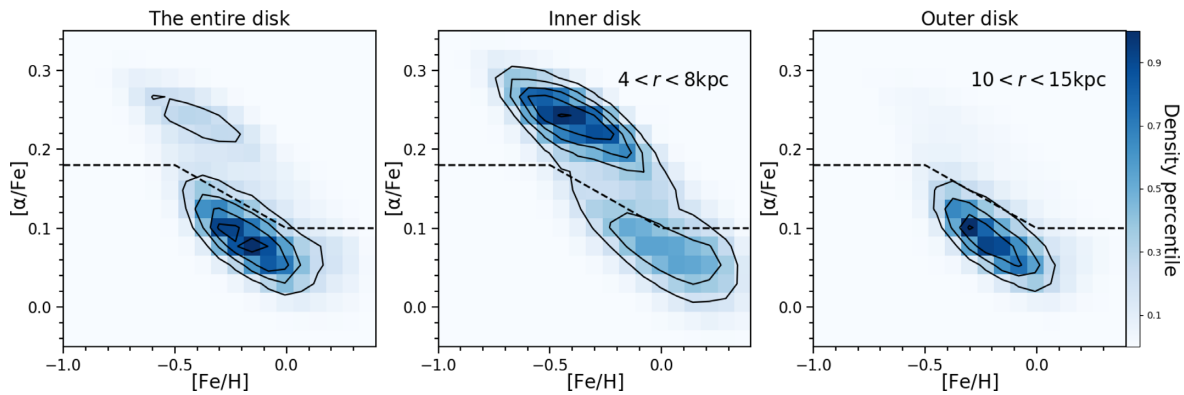


**Figure 2.** Density distribution of stars observed by APOGEE in the  $[\alpha/\text{Fe}]$ – $[\text{Fe}/\text{H}]$  plane, with contour lines, for the entire disk (left-hand panel), the inner disk ( $4 < r < 8$  kpc, middle panel), and the outer disk ( $r > 10$  kpc, right-hand panel). The bimodal distribution can be clearly seen, and the two populations are well separated. The dashed black line highlights the separation. In this work, we focus on the Galactic outer disc that is dominated by the low- $\alpha$  population (right-hand panel).

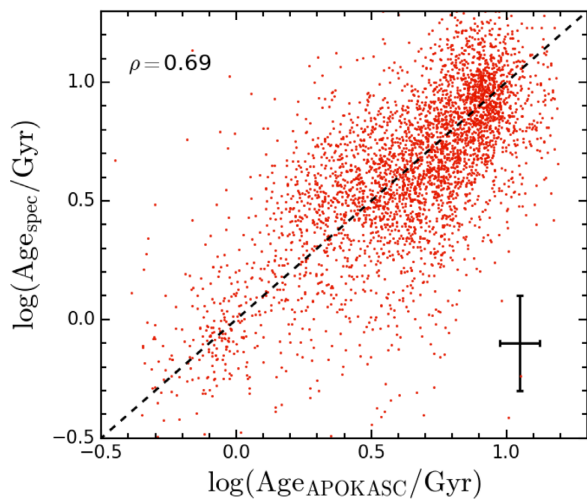


**Figure 3.** Comparison between the age based on a combination of asteroseismology and APOGEE spectroscopy (x-axis) with the age based on APOGEE spectra alone (y-axis). Typical uncertainties are indicated by the error bar in the bottom-right corner. The dashed line is the one-to-one relation. There is a good correlation between the two age measurements with a Pearson’s correlation coefficient of 0.69 (top-left corner). The average scatter is 0.26 dex.

average. This suggests the ages from Ness et al. (2016) used in this work are robust within an uncertainty of 0.26 dex.

Note that the scatter in Fig. 3 slightly decreases with increasing age. To account for the age-dependent uncertainty, we therefore estimate the uncertainties for following three age bins:

- (i) Age  $< 2.5$  Gyr [ $\log(\text{age}/\text{Gyr}) < 0.4$ ];
- (ii)  $2.5 < \text{age} < 6$  Gyr [ $0.4 < \log(\text{age}/\text{Gyr}) < 0.8$ ];
- (iii) Age  $> 6$  Gyr [ $\log(\text{age}/\text{Gyr}) > 0.8$ ].

The adopted scatter is summarized in Table 1. These errors are mainly caused by the relatively large uncertainties in the spectroscopic age measurements indicated by the error bar in Fig. 3.

### 2.3 Combined $[\alpha/\text{Fe}]$ – $[\text{Fe}/\text{H}]$ –age distribution

Because of the difficulty in measuring accurate stellar ages, the distribution of stars in the  $[\alpha/\text{Fe}]$ – $[\text{Fe}/\text{H}]$  plane is usually studied

**Table 1.** Uncertainties in the age determination.

Age bin (log/dex)	Scatter (log/dex)	Age bin (linear/Gyr)	Scatter (linear/Gyr)
$< 0.4$	0.3	$< 2.5$	1.8
0.4–0.8	0.22	2.5–6	2.3
$> 0.8$	0.19	$> 6$	4.2

without consideration of stellar ages. As discussed in the previous section, thanks to the combination of age determinations from spectroscopy and asteroseismology, stellar ages for large samples of stars beyond the solar neighbourhood have now become available. In this paper, we therefore aim at modelling age and chemical abundance *simultaneously*.

In this section, we discuss the observed distributions qualitatively and will then present the results from our chemical evolution model (described in Section 3) for a quantitative analysis in Section 4.

#### 2.3.1 $[\text{Fe}/\text{H}]$ versus $[\alpha/\text{Fe}]$

The left-hand panel of Fig. 4 shows the distribution of the outer disc stars in the  $[\text{Fe}/\text{H}]$ – $[\alpha/\text{Fe}]$  plane colour coded by mean stellar age in each  $[\text{Fe}/\text{H}]$ – $[\alpha/\text{Fe}]$  bin.

Two sequences with different ages can be identified separated by the dashed line: one sequence of young ( $\sim 2$  Gyr, blue colours) to intermediate-age ( $\sim 4$  Gyr, yellow colours) stars with systematically lower  $[\alpha/\text{Fe}]$  ratios by  $\sim 0.05$  dex and a sequence of intermediate-age to old ( $> 7$  Gyr, orange to red colours) stars with higher  $[\alpha/\text{Fe}]$ . We note that a similar two-age-sequence in the  $[\text{Fe}/\text{H}]$ – $[\alpha/\text{Fe}]$  plane for the low- $\alpha$  stars ( $[\alpha/\text{Fe}] < 0.15$ ) is also seen in disc stars observed by the LAMOST survey (see fig. 4 in Wu et al. 2018). Most surprisingly, the *younger* sequence (blue colours) is shifted towards *lower*  $[\text{Fe}/\text{H}]$ , resulting in an age–metallicity anticorrelation such that older stars are more metal rich.

This trend is the opposite of what is expected from simple chemical evolution with a single gas accretion phase. A single secular gas accretion phase is generally used to match the low- $\alpha$  sequence, such as the secular infall with long accretion time-scales in the original ‘two-infall’ model by Chiappini, Matteucci & Gratton (1997). An important prediction of this secular evolution process is a monotonic metal enrichment history leading to element abundances

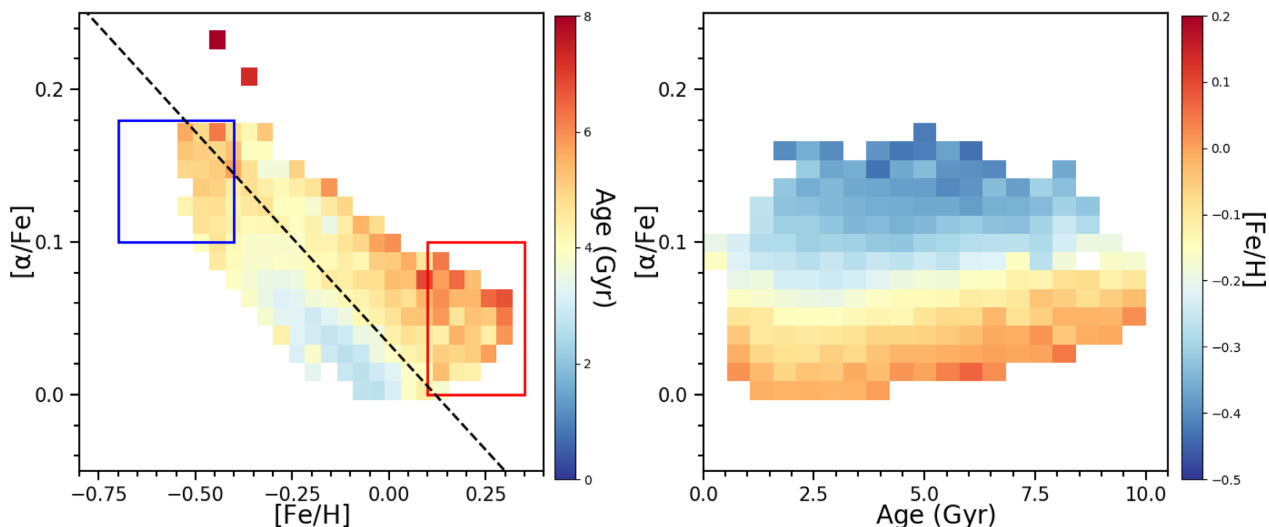


**Figure 4.** The outer disc stars in the three-dimensional parameter space of  $[\alpha/\text{Fe}]$ ,  $[\text{Fe}/\text{H}]$ , and age. *Left-hand panel:*  $[\alpha/\text{Fe}]$  as a function of  $[\text{Fe}/\text{H}]$  colour coded by mean stellar age. The dashed line separates the two sequences with different stellar ages. The blue and red boxes highlight the location of stars possibly formed at the beginning and at the end point of the late-accretion event, respectively. Their ages are used to estimate the start time and the time-scale of the late-accretion event. *Right-hand panel:*  $[\alpha/\text{Fe}]$  as a function of age colour coded by mean  $[\text{Fe}/\text{H}]$ . Two surprising features are present in the plot: (1) an age–metallicity anticorrelation (the presence of young stars with low  $[\text{Fe}/\text{H}]$  as well as old stars with high  $[\text{Fe}/\text{H}]$ ), and (2) the young metal-poor population is  $\alpha$ -enhanced (see more details in the text).

increasing monotonically with time (e.g. figs 13–17 in Anders et al. 2017). The presence of young metal-poor stars and old metal-rich stars is clearly in conflict with this model prediction. This trend suggests that the outer disc has experienced more than one major gas accretion event that perturbed its metal enrichment history. Most importantly, the young metal-poor stellar population must have formed in a metal-poor environment most plausibly caused by dilution with recently accreted, pristine gas.

### 2.3.2 Age versus $[\alpha/\text{Fe}]$

The right-hand panel of Fig. 4 illustrates this further. Here we plot  $[\alpha/\text{Fe}]$  as a function of age colour coded by  $[\text{Fe}/\text{H}]$ . There is no significant correlation between  $[\alpha/\text{Fe}]$  and age. But very interestingly, we notice the presence of a group of intermediate-age stars (age  $\sim 5$  Gyr) with relatively high  $\alpha$  abundance ( $0.1 < [\alpha/\text{Fe}] < 0.18$ ) and low iron abundance ( $[\text{Fe}/\text{H}] < -0.3$ ). The presence of young  $\alpha$ -enhanced stars in a much smaller sample was already reported by Martig et al. (2015) and Chiappini et al. (2015). A simple chemical evolution model cannot explain the formation of this stellar population.

The relatively young age and high  $\alpha/\text{Fe}$  ratio of these stars suggest that they were formed in a recent, relatively short star formation episode. The low iron abundance further implies that this starburst must have been accompanied or triggered by the accretion of pristine/metal-poor gas. Note that the iron abundance of these stars is lower than the iron abundance of older metal-rich ( $[\text{Fe}/\text{H}] > 0.1$ ) stars by  $\sim 0.5$  dex.

Within this scenario, the most metal-rich stars ( $[\text{Fe}/\text{H}] > 0.1$ , red box in the left-hand panel of Fig. 4) are the last population to form *before* the onset of dilution due to late accretion of metal-poor gas, while the most metal-poor stars ( $[\text{Fe}/\text{H}] < -0.4$ , blue box in the left-hand panel of Fig. 4) are the last population to form in the accretion itself. The two boxes in the left-hand panel highlight these stars that possibly formed at the start and end point of the late-accretion event. The stellar populations in the metal-rich (red)

and metal-poor (blue) boxes have average ages of  $5.5 \pm 3.1$  and  $4.8 \pm 1.9$  Gyr, respectively. This puts stringent constraints on the onset and duration of the late-accretion event.

In the following, we use a numerical chemical evolution model to explore and quantify this scenario.

## 3 THE CHEMICAL EVOLUTION MODEL

The chemical evolution model used in this work was initially developed to understand the origin of the mass–metallicity relation for both gas and stars of local galaxies (Lian et al. 2018a). The model was then expanded to explain the radial distribution of gas and stellar metallicity in local star-forming galaxies (Lian et al. 2018b, 2019) as well as the cosmic evolution of the mass–metallicity relation from  $z \sim 3.5$  to 0 (Lian, Thomas & Maraston 2018c). The model is designed to be generic and can be used to infer the chemical evolution in galaxies globally as well as in sub-regions within galaxies. In this work, we develop the model further to include the evolution of chemical element ratios to allow for a direct comparison with observations in our Galaxy. We refer the reader to these papers for a detailed description of the model. Here we provide a brief summary of key aspects relevant to this work.

### 3.1 Key parameters

The model considers three basic processes that regulate the chemical evolution of galaxies: star formation, gas accretion, and galactic winds. The initial gas accretion phase is assumed to decline exponentially. Two free parameters are used to describe the accretion phase, the initial accretion rate  $A_{\text{acc},i}$  and the e-folding time-scale  $\tau_{\text{acc}}$ . Star formation is implemented through the Kennicutt–Schmidt (KS) star formation law (SFL; Kennicutt 1998), which implies the SFR surface density to be proportional to the gas mass surface density through a power law as described by the following equation:

$$\Sigma_{\text{SFR}} = 2.5 \times 10^{-4} \times C_{\text{ks}} \times (\Sigma_{\text{gas}}/M_{\odot} \text{pc}^{-2})^{n_{\text{ks}}} M_{\odot} \text{yr}^{-1} \text{kpc}^{-2}.$$

We fix the power index  $n_{\text{ks}}$  to 1.5 for normal star-forming galaxies (Kennicutt et al. 2007), which is close to the original value of 1.4 obtained for starburst galaxies (Kennicutt 1998). The parameter  $C_{\text{ks}}$ , which regulates the star formation efficiency (SFE; star formation rate per unit gas mass), is normalized to the original coefficient of the KS law (i.e.  $2.5 \times 10^{-4}$ ) and is allowed to vary. Different SFE values were found for different galaxies and also within galaxies (e.g. Leroy et al. 2008; Zhang et al. 2019). The SFE may also increase with redshift. Lilly et al. (2013) find that an increase of the SFE with redshift explains the cosmic evolution of the mass–metallicity relation (however, see the recent review by Maiolino & Mannucci 2019 for other possible mechanisms). A varying SFE is possibly related to the balance between the gas phases of H I and H II on small scales. The formation of H II from H I as well as its destruction depends on the local small-scale environment (e.g. stellar surface density and metallicity; Leroy et al. 2008) that varies from galaxy to galaxy and even within individual galaxies.

Finally, we note that a Kroupa stellar initial mass function (Kroupa 2001) is adopted in the model.

### 3.2 Nucleosynthesis prescription

Metal production from asymptotic giant branch stars, Type-Ia supernovae (SN-Ia), and Type-II supernovae (SN-II) is included in the model, considering their different lifetimes. A detailed description of the yield table used in the model can be found in Lian et al. (2018a). The stellar yields of SN-II have been updated to the more recent work by Kobayashi et al. (2006).

To properly model  $[\alpha/\text{Fe}]$ , the SN-Ia rate needs to be taken into account carefully. One of the methods in the literature adopts a ‘first-principle’ approach to model the SN-Ia rate using a theoretical SN-Ia rate formalism (Greggio & Renzini 1983; Matteucci & Greggio 1986; Thomas, Greggio & Bender 1998). This approach requires assumptions of the progenitor type of SN-Ia, the binary mass function, the secondary mass fraction distribution at a given mass of the binary system, and binary lifetimes. Because of the uncertainties in the nature of SN-Ia progenitors, empirical SN-Ia delay-time distributions (DTDs) calibrated to the observed SN-Ia rates have been proposed (Strolger et al. 2004; Matteucci et al. 2006; Maoz, Mannucci & Brandt 2012). In this work, we adopt the power-law SN-Ia DTD proposed by Maoz et al. (2012) with a slope of  $-1.1$  as follows:

$$\text{DTD} = a(\tau/\text{Gyr})^{-1.1},$$

where  $\tau$  is the delay time since the birth of the SN-Ia-producing binary systems, and  $a$  is a normalization constant so that

$$\int_{\tau_{\min}}^{\tau_{\max}} \text{DTD}(\tau) d\tau = 1.$$

Here  $\tau_{\min} = \tau_{8\odot}$  and  $\tau_{\max} = \tau_{0.85\odot}$ , which are the minimum and maximum assumed lifetimes of an SN-Ia-producing binary, respectively. We will discuss the effect of different descriptions for the SN-Ia rate in Section 5.1.

### 3.3 Models for the MW disc

The success of our chemical evolution model at reproducing observations for a wide range in cosmic time and physical scale (Lian et al. 2018a,b,c) suggests that the key processes driving chemical evolution – star formation, gas inflow, and outflow – have been adequately taken into account. In this paper, we now expand this model further to constrain the detailed chemical enrichment

history of our Galaxy through comparison with observations of individual stars.

By modelling gas and stellar metallicities of local star-forming galaxies, we found that the strength of metal outflow (i.e. the metal mass loading factor) depends on a galaxy’s total stellar mass and plays a relatively unimportant role in the chemical evolution of massive star-forming galaxies with a stellar mass above  $10^{10.5} M_{\odot}$  (Lian et al. 2018a,b). We assume a today’s stellar mass of  $\sim 6 \times 10^{10} M_{\odot}$  for our Galaxy (McMillan 2011). Therefore, no metal outflow is assumed here for the MW. To keep the model generic, we calculate the chemical evolution within a squared area of size of  $1 \text{ kpc}^2$ . The size of the area can be considered as a normalization factor of the model. All parameters in our model are calculated per unit area and are therefore expressed in units of  $\text{kpc}^{-2}$ . To get results for a particular area, the values of our output parameters need to be scaled accordingly. The values for the entire outer disc are obtained by multiplication with the area of the outer disc. For example, the initial gas accretion rate for the entire outer disc equals the initial accretion rate ( $0.007 M_{\odot} \text{ yr}^{-1} \text{ kpc}^{-2}$  in the late-accretion model) times the area of the outer disc ( $392.7 \text{ kpc}^2$  for an annulus with a radius between 10 and 15 kpc), which is  $2.75 M_{\odot} \text{ yr}^{-1}$ . In the same way, we estimate the total gas mass accreted in the late-accretion event. We implicitly assume the outer disc to be homogeneous in stellar chemical abundances. This is supported by the spatially resolved  $[\alpha/\text{Fe}]$ – $[\text{Fe}/\text{H}]$  diagram in fig. 4 in Hayden et al. (2015) that shows insignificant radial variation within the outer disc. A more detailed study of abundance variation across the Galactic disc (e.g. the metallicity gradient) will be presented in future work. The time resolution of the model is 0.05 Gyr.

To perform a more direct comparison with the data, we simulate the stellar distribution predicted by the model after considering stellar mass-loss. The observational uncertainties of  $[\alpha/\text{Fe}]$  and  $[\text{Fe}/\text{H}]$  are  $\sim 0.02$  dex on average (Ness et al. 2016). We adopt these uncertainties and the age-dependent uncertainty of age from Table 1.

As discussed in Section 2.3, an additional phase of recent gas accretion on top of the secular accretion phase is required to explain the observed distribution of outer disc stars in the  $[\alpha/\text{Fe}]$ – $[\text{Fe}/\text{H}]$ –age space. We explore this scenario quantitatively with a model adopting an additional short accretion event on top of the underlying secular accretion. We refer to this model as ‘late-accretion model’. For comparison, we also consider a model assuming a single exponentially declining accretion phase referred to as ‘single- $\tau$  model’.

In the late-accretion model, the additional accretion event is characterized by the time of accretion  $t_{\text{acc}}$ , the accretion time-scale  $t_{\text{d}}$ , the accretion rate  $A_{\text{acc}}$ , and an enhanced SFE achieved by an increased value for the coefficient of the KS law during the event  $C_{\text{ks, acc}}$ .

As discussed in Section 2.3, the time of accretion  $t_{\text{acc}}$  is mostly constrained by the age of the observed most metal-rich stars and the accretion time-scale is given by the age difference between these and the most-poor stars. The observational data imply the average age of the most metal-rich stars to be  $5.5 \pm 3.1$  Gyr and of the most metal-poor stars to be  $4.8 \pm 1.9$  Gyr. This provides us with an estimate for  $t_{\text{acc}}$  and  $t_{\text{d}}$  and their uncertainties.

The accretion rate  $A_{\text{acc}}$  is constrained by the difference in  $[\text{Fe}/\text{H}]$  of the stars formed before and during accretion, i.e. the decrease in  $[\text{Fe}/\text{H}]$  due to dilution. The dilution effect is well constrained as the stars formed before and after the accretion event are observed.

The enhanced coefficient of the KS law  $C_{\text{ks, acc}}$  is largely constrained by the enhancement of  $[\alpha/\text{Fe}]$  during the accretion

**Table 2.** Parameters adopted for the model with a single accretion phase and a set of late-accretion models with different accretion time-scales  $t_d$ . The subscript ‘i’ stands for initial value of the parameter and ‘acc’ stands for the parameter adopted during the late-accretion event.  $C_{ks, after}$  is the star formation law coefficient after the late-accretion event.

	$A_{acc, i}$ $M_{\odot} \text{ yr}^{-1} \text{ kpc}^{-2}$	$\tau_{acc, i}$ Gyr	$t_{acc}$ Gyr	$t_d$ Gyr	$C_{ks, i}$	$C_{ks, acc}$	$A_{acc}^a$ $M_{\odot} \text{ yr}^{-1} \text{ kpc}^{-2}$	$C_{ks, after}$	$[\text{Fe}/\text{H}]_{acc}$ dex
Single- $\tau$	0.002	10	–	–	0.50	–	–	–	–
$t_d = 0.05$ Gyr	0.007	2	8.2	0.05	0.60	2.80	0.300	0.45	pristine
$t_d = 0.7$ Gyr (Fiducial)	0.007	2	8.2	0.7	0.60	0.85	0.024	0.14	pristine
$t_d = 1.5$ Gyr	0.007	2	8.2	1.5	0.60	0.60	0.020	0.10	pristine
Continuous acc	0.007	2	8.2	–	0.60	0.60	0.024	–	pristine
$t_d = 0.7$ Gyr	0.007	2	8.2	0.7	0.60	0.85	0.036	0.14	–1

<sup>a</sup>Constant accretion rate is assumed during the late-accretion event except for the continuous accretion model in which the accretion rate declines exponentially with an e-folding time of 8 Gyr.

event ( $0.06 < [\alpha/\text{Fe}] < 0.13$  dex). As we will show later, less enhancement in SFE is required in case of a longer accretion time-scale. Table 2 summarizes the model parameters.

The parameters adopted for the single- $\tau$  model and the late-accretion models with various  $t_d$  for the outer disc are listed in Table 2. The additional late accretion in the fiducial late-accretion model occurs at a look-back time of 5.5 Gyr corresponding to a cosmic time of 8.2 Gyr or  $z \sim 0.6$ .  $1.68 \times 10^7 M_{\odot} \text{ kpc}^{-2}$  pristine gas is accreted. For comparison, Spitoni et al. (2019) adopt an earlier second gas accretion at a larger look-back time of 9.4 Gyr (or cosmic time of 4.3 Gyr).

The coefficient of the star formation law is enhanced by a factor of 1.4. Based on the age difference between the most metal-rich and most metal-poor populations, we adopt an accretion time-scale of 0.7 Gyr in the fiducial late-accretion scenario, assuming a constant accretion rate during accretion.

We test this choice by exploring various late-accretion models with different accretion time-scales (see Section 4 and Figs 5 and 6). It should also be noted that the observed peak in  $[\alpha/\text{Fe}]$  can be matched with lower SFL coefficient in models with longer accretion time-scales. For an accretion with a time-scale as long as 1.5 Gyr, an enhancement in SFL coefficient is no longer needed. This is because a larger total amount of gas has to be accreted in models with longer accretion time-scales, in order to reach the same level of net dilution because of the additional chemical enrichment during the accretion episode itself.

The final stellar mass surface density and gas mass fraction of the fiducial late-accretion model are  $12.3 M_{\odot} \text{ kpc}^{-2}$  and 41 per cent, respectively. Assuming a disc scale length of 2.6 kpc (Bland-Hawthorn & Gerhard 2016) and a solar stellar mass surface density of  $33.4 M_{\odot} \text{ pc}^{-2}$  (McKee, Parravano & Hollenbach 2015), the stellar mass surface densities at the galactocentric radii of 10 and 15 kpc are  $15.5$  and  $2.3 M_{\odot} \text{ pc}^{-2}$ , respectively. Adopting the radial distribution of the gas mass surface density from Wolfire et al. (2003), we estimate the gas mass fraction (i.e.  $\frac{M_{\text{gas}}}{M_{\text{gas}} + M_{\text{star}}}$ ) within the radii of 10–15 kpc to be 28–68 per cent. Our results are well in line with these estimates.

## 4 RESULTS

In this section, we describe in detail the predictions of our models and compare them to observations.

### 4.1 Predicted evolutionary histories

Fig. 5 shows the evolution of gas accretion rate (top-left panel), star formation rate (top-right panel),  $[\text{Fe}/\text{H}]$  (bottom-left panel), and

$[\alpha/\text{Fe}]$  (bottom-right panel) as predicted by various late-accretion models with different accretion time-scales  $t_d$  as well as the single accretion model. We adopt an exponentially declining time-scale of 8 Gyr for the continuous late accretion that is taken from Spitoni et al. (2019).

The late-accretion models are based on a secular accretion phase with  $\tau_{acc, i} = 2$  Gyr to which a second, late gas accretion event is added on top. The initial secular accretion phase is not well constrained due to lack of observed old stars with age  $> 8$  Gyr that formed during this phase in the outer disc. As a consequence, there is a degeneracy between the parameters characterizing this phase, including the initial gas accretion rate, the accretion time-scale, and the initial SFE. This degeneracy can be broken using observations in the inner Galaxy for which observational data of old stars are available. An improved model using data from the inner discs to constrain this early accretion phase will be presented in companion papers on the inner disc and bulge (Lian et al., in preparation).

In our model, the initial secular and the late-accretion events are independent of each other. The late-accretion event, unlike the underlying smooth accretion, is designed to occur abruptly on a short time-scale (0.7 Gyr in our fiducial model). This is required to boost the  $[\alpha/\text{Fe}]$  in the ISM. With the combination of an enhanced SFE, a starburst is induced for this accretion event (top-right panel of Fig. 5).

This late-accretion event affects the chemical enrichment significantly. Individual element abundances, such as  $[\text{Fe}/\text{H}]$ , are diluted dramatically, resulting in a sharp drop in its abundance (bottom-left panel of Fig. 5). For the same reason the  $\alpha$ -element abundances also drop initially by the same factor. However, because of the starburst that is triggered at the same time, the  $\alpha$ -abundance is boosted through chemical enrichment from short-lived Type-II supernova. As a result, the  $[\alpha/\text{Fe}]$  ratio peaks when the accretion event occurs (bottom-right panel of Fig. 5).

To summarize, there are three major effects induced by the late-accretion event: (1) a burst of star formation, (2) a suppression of iron abundance, and (3) an enhancement of the  $[\alpha/\text{Fe}]$  abundance ratio. These features create the key difference between the predictions of the late-accretion models and the single- $\tau$  model.

### 4.2 $[\alpha/\text{Fe}]$ – $[\text{Fe}/\text{H}]$ diagram

Fig. 6 shows the comparison of the single- $\tau$  and late-accretion models with observations in the  $[\alpha/\text{Fe}]$ – $[\text{Fe}/\text{H}]$  plane. The black contours indicate the observed data while the coloured lines are the predicted model tracks. The colour scheme is the same as in Fig. 5. The top-left panel summarizes the evolutionary trajectories of the different models while other panels visualize the predicted

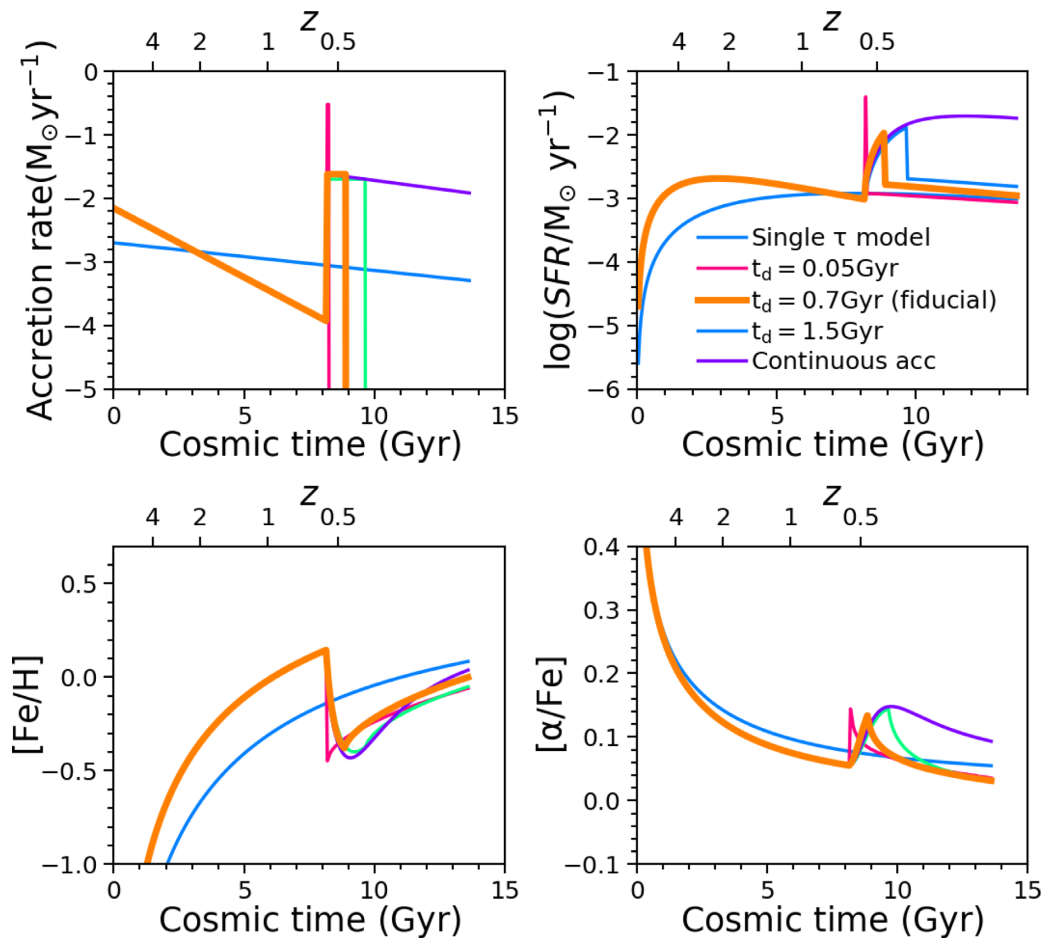


**Figure 5.** Gas accretion (top-left), star formation (top-right), iron abundance  $[\text{Fe}/\text{H}]$  (bottom-left), and  $[\alpha/\text{Fe}]$  abundance ratio (bottom-right) as a function of cosmic time for late-accretion models with different accretion time-scales  $\tau_d$  as well as the single- $\tau$  model (with single phase of gas accretion). Our fiducial model is a late-accretion model with a second infall time-scale of 0.7 Gyr. The time-scale of the secular gas accretion phase is 10 Gyr in the single- $\tau$  model and 2 Gyr in the late-accretion models. The late-accretion models are based on a modified single- $\tau$  model with an additional accretion event imposed on top of the secular accretion. The accretion decreases the  $[\text{Fe}/\text{H}]$  abundance, but the starburst that is triggered by the accretion still manages to enhance the  $[\alpha/\text{Fe}]$ .

distributions of the stellar abundances for each model (coloured dots) after considering the observational uncertainties. An uncertainty of 0.02 dex for  $[\alpha/\text{Fe}]$  and  $[\text{Fe}/\text{H}]$  is adopted. The age uncertainty is summarized in Table 1. The beginning and the end of the late gas accretion episode in the fiducial late-accretion model are marked with black squares.

It can be seen that the single- $\tau$  model track appears to match the observed trend equally well as the late-accretion models in the  $[\alpha/\text{Fe}]$ – $[\text{Fe}/\text{H}]$  plane. This model is similar to the models generally used in the literature to explain the chemical compositions of thin disc stars (e.g. Chiappini 2009; Anders et al. 2017). This is challenged, however, by the distribution of stellar abundances in this diagram that peaks at a lower  $[\text{Fe}/\text{H}]$  and appears to be more symmetric. It can be seen that the latter is best matched by the fiducial late-accretion model (bottom-left panel).

It is also interesting to note that the distribution in  $[\alpha/\text{Fe}]$ – $[\text{Fe}/\text{H}]$  as predicted by the late-accretion model is actually composed of two parallel evolutionary sequences, one before and one after the accretion event. The first sequence consists of stars formed from gradually accreted gas prior to the accretion episode and the other is made of stars formed during and after the late accretion. These two  $[\alpha/\text{Fe}]$ – $[\text{Fe}/\text{H}]$  sequences of stars with different ages are in

good agreement with the observed age–chemical structure shown in Fig. 4.

#### 4.3 $[\alpha/\text{Fe}]$ – $[\text{Fe}/\text{H}]$ –age relation

In the previous section, we compared model and data in the  $[\alpha/\text{Fe}]$ – $[\text{Fe}/\text{H}]$  diagram without age information. Here we add age as a further parameter as shown in Fig. 7. For simplicity, we only include the single- $\tau$  and the fiducial late-accretion model. The top row shows the  $[\alpha/\text{Fe}]$ – $[\text{Fe}/\text{H}]$ , and the bottom row the  $[\alpha/\text{Fe}]$ –age planes, respectively (see Fig. 4). The left-hand column shows the observational data, and the middle and right-hand columns show the predicted distributions from the fiducial late-accretion model and the single- $\tau$  model, respectively. The black dashed lines in the top panels separate the two  $[\alpha/\text{Fe}]$ – $[\text{Fe}/\text{H}]$  sequences with different ages (see Fig. 4).

It can be seen that the observed distribution in  $[\alpha/\text{Fe}]$ – $[\text{Fe}/\text{H}]$ –age is well reproduced by the fiducial late-accretion model. The two  $[\alpha/\text{Fe}]$ – $[\text{Fe}/\text{H}]$  sequences with different ages seen in the observations (top-left panel) are well matched (top-middle panel). In particular, the observed age–metallicity anticorrelation visible



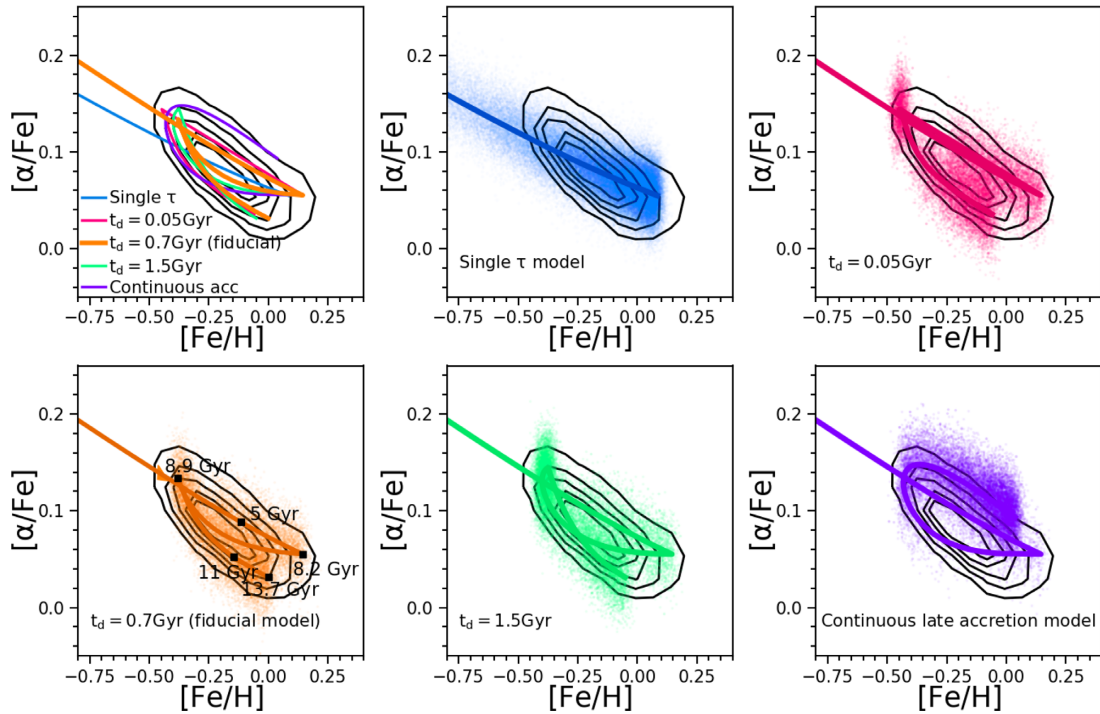


**Figure 6.** Comparison of model predictions with observational data in the  $[\alpha/\text{Fe}]$ – $[\text{Fe}/\text{H}]$  plane. The black contours show the observed distribution while the lines are the model tracks with the same colour scheme as in Fig. 5. The coloured dots in each panel are the simulated distributions after considering observational uncertainties. Five epochs at 5, 8.2, 8.9, 11, and 13.7 Gyr in the fiducial late-accretion model are marked as black squares for reference.

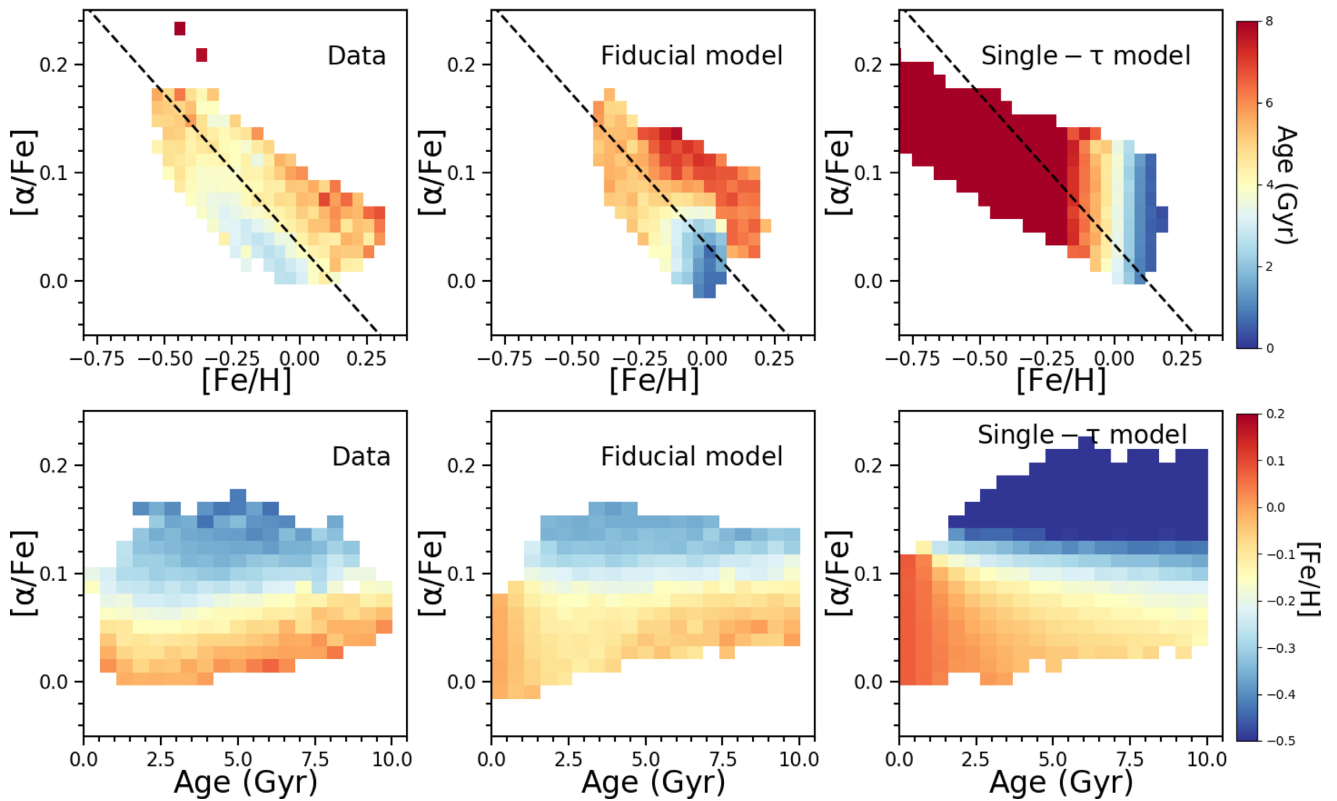


**Figure 7.** Comparison of model predictions with observational data in the  $[\alpha/\text{Fe}]$ – $[\text{Fe}/\text{H}]$  plane colour coded by mean age (top row) and in the  $[\alpha/\text{Fe}]$ –age plane colour coded by mean  $[\text{Fe}/\text{H}]$  (bottom row). Columns from left to right are observations, late-accretion model, and single- $\tau$  model, respectively. The black dashed line in the top panels separates the two sequences in the  $[\alpha/\text{Fe}]$ – $[\text{Fe}/\text{H}]$  plane (see Fig. 4).

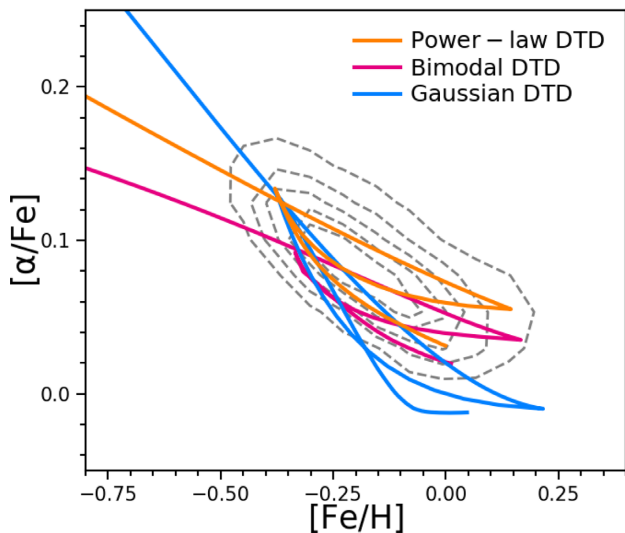


**Figure 8.** Late-accretion models with different descriptions for the SN-Ia rate based on different delayed-time distributions (DTD). Parameters in these models are identical as listed in Table 2.

through the presence of old metal-rich and young metal-poor stars is matched by the fiducial late-accretion model.

This model also reproduces the presence of intermediate-age ( $2 < t < 6$  Gyr), metal-poor ( $[\text{Fe}/\text{H}] < -0.25$ ) stars with relatively high  $[\alpha/\text{Fe}]$  ratios ( $[\alpha/\text{Fe}] \sim 0.14$ ) as shown in the bottom panels. As discussed above, these stars are the first generation formed during the starburst triggered by the late-accretion event.

The single- $\tau$  model (right-hand panels), instead, fails to reproduce the complex age–element abundance structure. As ought to be expected, this model predicts  $[\text{Fe}/\text{H}]$  to increase monotonically with decreasing age (hence increasing cosmic time), accompanied by a decreasing  $[\alpha/\text{Fe}]$  ratio. As a result, only a single evolutionary sequence is present in the  $[\alpha/\text{Fe}]$ – $[\text{Fe}/\text{H}]$  plane. All stars with high  $[\alpha/\text{Fe}]$  are predicted to form at early times with old ages, in contrast to what is observed.

To summarize, the two-phase disc formation scenario with a delayed second accretion event as described by the fiducial late-accretion model provides a much better fit to the observed age–element abundance structure of the outer disc. The simple model based on a single phase of secular evolution fails.

## 5 DISCUSSION

In this section, we will discuss uncertainties, implications, and predictions of our late-accretion model and confront with alternative scenarios in the literature.

### 5.1 The late-accretion model

#### 5.1.1 The effect of different SN-Ia DTDs

It is easy to understand that the evolution of  $[\alpha/\text{Fe}]$  is sensitive to the description of the SN-Ia rate that dominates the production of iron. Fig. 8 shows models with the same parameter configuration as before but with different DTDs (power-law DTD, Maoz et al. 2012; bimodal DTD, Matteucci et al. 2006; Gaussian DTD, Strolger et al. 2004). It can be seen that the  $[\alpha/\text{Fe}]$  values are affected by up to  $\sim 0.1$  dex at a given  $[\text{Fe}/\text{H}]$ . Nevertheless, the overall evolutionary trends in the  $[\alpha/\text{Fe}]$ – $[\text{Fe}/\text{H}]$  plane as predicted by these different

models are broadly consistent. Although the parameters adopted in our late-accretion model are subject to small changes for different DTDs, the main result of this paper, namely that a late-accretion event is required to explain the age–chemical abundance structure of the outer disc, remains unchanged. Moreover, it is worth pointing out that some key parameters that characterize the late-accretion event are determined directly by the observations and are therefore not affected by changes of the DTD or other model configurations, including the onset time (8.2 Gyr) and time-scale (0.7 Gyr) of the late-accretion episode. Likewise, the fraction of pristine gas accreted is well constrained by observations.

#### 5.1.2 Late accretion: a galaxy merger?

In this paper, we show that an additional, short accretion episode delayed by  $\sim 8.2$  Gyr is required to explain the complex age–element abundance structure of the Galactic outer disc. Our model suggests that the accreted gas is not connected to the underlying secular gas accretion. We further find that the mass of accreted gas needs to exceed the mass of the local gas reservoir in the outer disc by a factor of 3. These characteristics disfavour quasi-continuous gas accretion from the circumgalactic medium and suggest that the late-time gas accretion may be caused by the accretion of a gas-rich dwarf galaxy. As in a minor merger, the accretion of gas generally happens earlier than the accretion of stars through ram pressure processes, the stellar component of the infalling galaxy may not be fully disrupted yet. Interestingly, recent simulations by Tepper-García & Bland-Hawthorn (2018) suggest that the massive stripping of gas from the infalling Sagittarius dwarf galaxy (Ibata, Gilmore & Irwin 1994) started  $\sim 3$  Gyr ago, which makes Sagittarius a promising candidate for being the accreted galaxy leading to the late-accretion episode discussed in this paper.

The model presented here allows us to infer several key properties of the accreted galaxy. Since the lowest iron abundance of the stars formed during the accretion event is  $\sim -0.5$  dex, the iron abundance in the gas of the accreted galaxy would have to be lower than  $-0.5$  dex to be able to dilute the gas in the outer Galactic disc. This upper limit in metallicity can be translated to an upper limit in stellar mass of the accreted galaxy. Using the observed (stellar) mass–(gas-phase) metallicity relation of galaxies at intermediate redshifts (i.e.  $z \sim 0.3$ – $0.7$ ; Savaglio et al. 2005; Lian et al. 2016), we find this upper mass limit to be  $M_* \sim 10^9 M_\odot$ . The stellar mass of Sagittarius is estimated to be a few times  $10^8 M_\odot$  (Gibbons, Belokurov & Evans 2017), which is well consistent with the upper limit estimated here.

Assuming that the gas (and the subsequently formed stars) of the accreted galaxy settled evenly in the outer disc around  $10 < r < 15$  kpc (the region we are analysing in this paper), the required gas mass of the accreted galaxy would have to be  $3 \times 10^9 M_\odot$ . Combining this with the estimate of the stellar mass based on the mass–metallicity relation above, the gas fraction of the accreted galaxy is estimated to be  $\sim 75$  per cent. The merger hypothesis advocated here would therefore imply the system accreted by our Galaxy to be a gas-rich dwarf galaxy.

#### 5.1.3 Disc flaring

The thickness of the Galactic disc (i.e. its scale length) is generally found to be constant with radius (Bovy, Rix & Hogg 2012; Bovy et al. 2012b). However, this is not the case for sub-populations in the disc. The scale height of the young sub-component increases with increasing radius, which is usually referred to as ‘flaring’

(Kalberla et al. 2014; Carraro et al. 2015). By analysing the spatial structure of mono-abundance populations, Bovy et al. (2016) and Mackereth et al. (2017) systematically studied thickness and flaring as a function of  $[\alpha/\text{Fe}]$  and  $[\text{Fe}/\text{H}]$ . It turns out that flaring is complex and depends on chemical abundances. In general, the flaring amplitude is negligible for the high- $\alpha$  population but significant for the low- $\alpha$  population. Moreover, within the low- $\alpha$  population, flaring is most pronounced for the most metal-poor population with  $[\text{Fe}/\text{H}] \sim -0.5$  dex.

Radial migration is one of the mechanisms believed to be responsible for flaring. The idea is that the stars moving outward face less gravitational pull in the outer disc and therefore move to larger vertical distances. However, to explain the dependence of flaring on the element abundances as discussed above, a contrived mechanism for radial migration would be required.

The late-accretion model presented here provides an alternative scenario for explaining the flaring in the low- $\alpha$  population. Our model implies that the most metal-poor, low- $\alpha$  population forms during a recent, merger-induced starburst. The large scale height of this population could then well be caused by the hot kinematics of the gas that fuels the starburst. A larger vertical scale height of this population in the outer disc is indeed expected, if the strength of the starburst and the associated gas accretion is more pronounced at large radii. This would lead to the observed flaring pattern.

#### 5.1.4 Kinematics

In the following, we briefly investigate the observed kinematic properties of stars in the outer disc in light of the proposed late-accretion model. Fig. 9 shows the distribution of four kinematic properties (maximum total orbit energy  $E_{\text{max}}$ , radial velocity  $U$ , vertical velocity  $W$ , and rotation velocity  $V$ ) in the  $[\alpha/\text{Fe}]$ – $[\text{Fe}/\text{H}]$  plane. These kinematic parameters are taken from a synergistic catalogue of APOGEE and *Gaia*.

The orbit information of each star is derived with the GRAVPOT16 code<sup>2</sup> based on a 3D steady-state gravitational potential model for the Galaxy, modelled as the sum of axisymmetric and non-axisymmetric components (Fernandez-Trincado et al., in preparation). The axisymmetric component is made up of the superposition of many composite stellar populations from the thin disc and a contribution from the thick disc. The density profile of the thin disc component is assumed to follow the Einasto laws (Einasto 1979), while a  $\text{sech}^2$  law is adopted for the density profile of the thick disc component. The non-axisymmetric component is modelled by a ‘boxy/peanut’ bar structure whose density profile is observationally constrained from the 2MASS data (see Robin et al. 2012). These stellar components are assumed to be surrounded by an isothermal dark matter halo component with a mass density as presented in Robin et al. (2003).

For the computation of Galactic orbits, we employ a simple Monte Carlo approach and the Runge–Kutta algorithm of seventh-order. For each APOGEE star, a thousand orbits are computed backward in time during 3 Gyr. As to the input parameters, we use the sky positions and line-of-sight velocities from the APOGEE survey. The proper motions and spectrophotometric distances are adopted from *Gaia* DR2. The spectrophotometric distances from *StarHorse* are relatively precise even out to large distances.

Within the low- $\alpha$  sequence, the metal-poor populations (below the dashed line) and the metal-rich populations (above the dashed

line) show systematically different kinematic properties. The total orbit energy in the metal-poor stars is generally higher than the total orbit energy in the metal-rich stars, which is mainly caused by their faster rotation velocities. The metal-poor stars also tend to have non-zero radial and higher vertical velocities than the metal-rich stars. All these differences suggest that the metal-poor populations likely formed from gas with hotter kinematics. This is qualitatively in line with the dynamical effect of a gas-rich merger event. The latter is expected to lead to vigorous star formation in a dynamically hot environment with complicated kinematics (Mihos & Bothun 1998; Colina, Arribas & Monreal-Ibero 2005).

Interestingly, a merger event between the MW and a dwarf galaxy named Gaia-Enceladus was recently identified (Helmi et al. 2018). This discovery is based on the peculiar velocity distribution of stars accreted from the dwarf galaxy with respect to the normal disc stars in the MW.

#### 5.1.5 Non-pristine accretion

In our fiducial late-accretion model, we assume the additional accreted gas to be pristine. We now explore whether and how our results will be affected if the accretion is already metal enriched to some extent. To this end, we assume  $[\text{Fe}/\text{H}] = 0.1$  dex for the accreted gas with a solar element abundance pattern. The comparison between the model prediction and observations in the  $[\alpha/\text{Fe}]$ – $[\text{Fe}/\text{H}]$  plane is shown in Fig. 10. It can be seen that the model prediction matches the data equally well. The best-fitting parameters adopted for this model are listed in Table 2. Compared to the fiducial model with pristine gas accretion, more gas accretion (50 per cent) is needed in order to dilute the iron abundance to the same value as before.

## 5.2 Alternative scenarios

In the following, we discuss other scenarios proposed in the literature.

### 5.2.1 Radial migration

The main reason why the single- $\tau$  model fails in matching observations is that element abundances increase with time in this model. This leads to a monotonic age–metallicity relation. This prediction is in disagreement with the observed complex age–element abundance structure of the Galactic outer disc. Most importantly, the coexistence of young, metal-poor and old, metal-rich populations cannot be understood with monotonic chemical enrichment.

The APOGEE data show that the stars in the Galactic inner disc are generally older and more metal rich than the stars in the outer disc. Still, the outer disc also contains a fraction of old, metal-rich stars very similar to the ones on the inner disc (Hayden et al. 2015). Hence, it may be possible that these stars originally formed in the inner disc and migrated to the outer disc over time (Feuillet et al. 2018). Such radial migration is indeed seen in simulations and is thought to play an important role in re-distributing stars in the MW (Schönrich & Binney 2009; Minchev, Chiappini & Martig 2013).

To test whether radial migration can explain the observed age–element abundance pattern in the outer disc, we run a version of the single- $\tau$  model in which the effect of radial migration is included. To model the chemical enrichment at different radial bins, we

<sup>2</sup><https://gravpot.utinam.cnrs.fr>

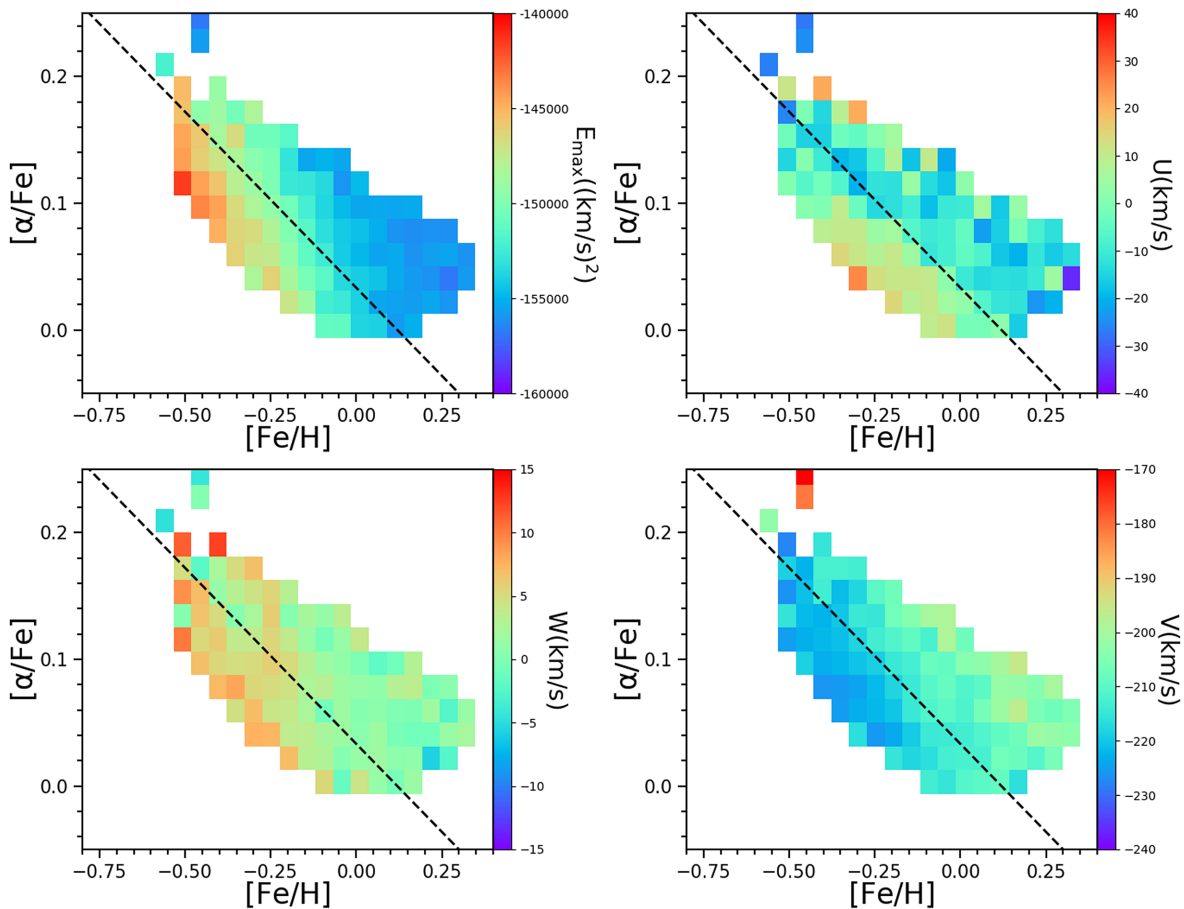


**Figure 9.** Distribution of the kinematic properties of stars in the  $[\alpha/\text{Fe}]$ – $[\text{Fe}/\text{H}]$  plane. *Top-left panel:* maximum total orbit energy. *Top-right panel:* radial velocity  $U$ . *Bottom-left panel:* vertical velocity  $W$ . *Bottom-right panel:* rotation velocity  $V$ .

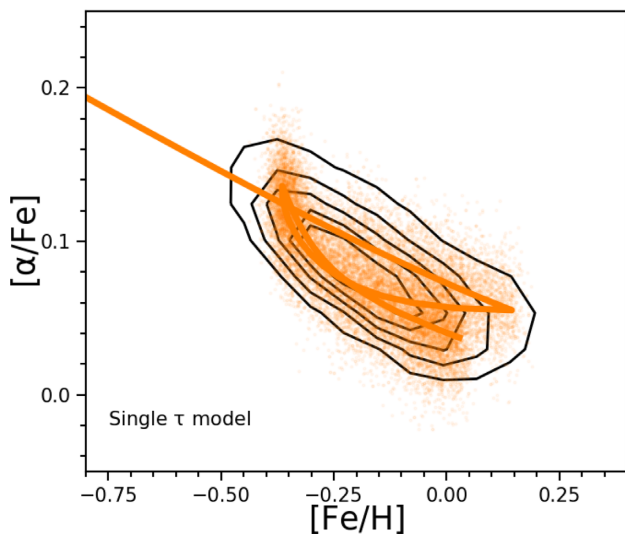


**Figure 10.** The same as the bottom-left panel of Fig. 6 but assuming that the additional gas accretion has been enriched to 10 per cent of solar abundance.

follow the approach of Chiappini, Matteucci & Romano (2001). We assume a single gas accretion phase with the accretion time-scale increasing linearly with increasing radius. We calculate a set of seven models with the gas accretion time-scale ranging from 2

to 14 Gyr. According to Chiappini et al. (2001), this corresponds to a range in radius from 3 to 15 kpc. The decrease in stellar mass density with increasing radius is considered in these models. The evolutionary tracks of age versus  $[\alpha/\text{Fe}]$  as predicted by the resulting model are shown in the left-hand panel of Fig. 11.

We then include the effect of radial migration by implementing a mass exchange between adjacent radial bins. At each time-step, a certain fraction of stars is set to move towards adjacent radial bins both outward and inward. The time-step assumed here is 1 Gyr and the fraction is 20 per cent. We verified that the results do not depend much on the exact values of these two parameters. The radial migration fraction of 20 per cent per Gyr is relatively high and broadly consistent with cosmological simulations (Ma et al. 2017).

The centre-left panel of Fig. 11 shows the resulting distribution in the  $[\alpha/\text{Fe}]$ –age plane colour coded by  $[\text{Fe}/\text{H}]$  for the radial bin with an accretion time-scale of  $\tau = 10$  Gyr. This roughly corresponds to a radius of 11 kpc. The centre-right and right-hand panels show the final distributions in the  $[\alpha/\text{Fe}]$ –age and  $[\alpha/\text{Fe}]$ – $[\text{Fe}/\text{H}]$  planes, respectively, taking into account the observational uncertainties.

This model does not perform significantly better than the original single- $\tau$  model. The monotonic increase of  $[\alpha/\text{Fe}]$  and  $[\text{Fe}/\text{H}]$  with cosmic time is still clearly visible. Even though radial migration adds some fraction of old metal-rich stars from the inner disc to the outer disc, which perturbs the distribution in  $[\alpha/\text{Fe}]$ –age and  $[\alpha/\text{Fe}]$ – $[\text{Fe}/\text{H}]$ , the improvement is marginal.

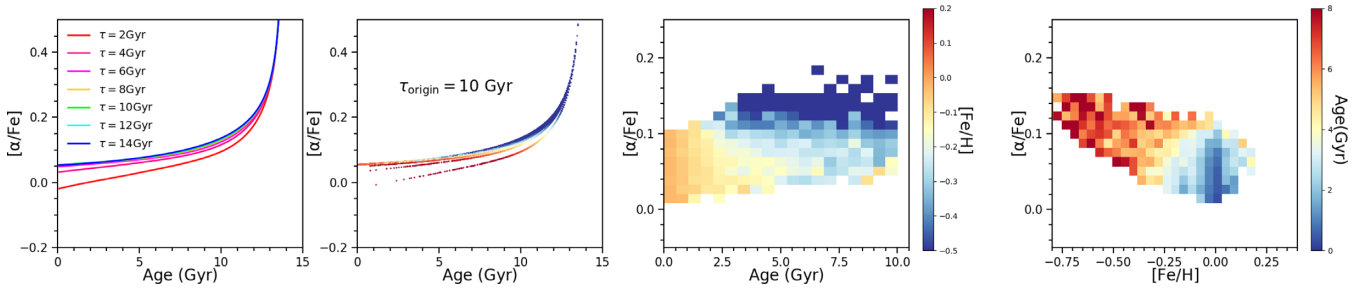


**Figure 11.** Theoretical predictions of the single- $\tau$  model including effects of radial migration. *Left-hand panel:*  $[\alpha/\text{Fe}]$  as a function of age showing seven models with different gas accretion time-scales from 2 to 14 Gyr for different radial bins. The shortest time-scale is used for the inner-most radial bin and increases with radius. *Centre-left panel:* Predicted distribution in the  $[\alpha/\text{Fe}]$ –age plane colour coded by  $[\text{Fe}/\text{H}]$  for the model of the radial bin at 11 kpc including the effects of radial migration (see the text for details). *Centre-right and right-hand panels:* Predicted distribution in  $[\alpha/\text{Fe}]$ –age and  $[\alpha/\text{Fe}]$ – $[\text{Fe}/\text{H}]$ , respectively, after considering observational uncertainties and selection effects.

We conclude that radial migration mitigates but does not fully resolve the difficulties of the single- $\tau$  model in matching the observational data.

Further evidence against radial migration playing a major role comes from the radial distribution. Assuming a constant radial migration efficiency with time, a larger scale length with a wider radial distribution would be expected for older populations simply because they have had more time to migrate. However, Bovy et al. (2012b, 2016) find the scale length for the old metal-rich stars in the low- $\alpha$  sequence to be small ( $\sim 2$  kpc). This scale length is similar to the one of the old stars in the high- $\alpha$  sequence but systematically smaller than the one of the younger metal-poor populations in the low- $\alpha$  sequence ( $\sim 4$  kpc).

### 5.2.2 The modified two-infall model

Spitoni et al. (2019) developed a modification of the classical ‘two-infall’ model in parallel to this work. Similar to our late-accretion model, their model proposes a second phase of gas accretion delayed by 4.3 Gyr. This second accretion phase is responsible for the formation of low- $[\alpha/\text{Fe}]$  stars. This modified ‘two-infall’ model is indeed able to reproduce the observations better. Indeed, this model is similar to our late-accretion model in that the second phase of gas accretion is delayed by several Gyr. However, fundamental differences remain.

First, the delayed accretion in our model is pushed to much later epochs than in Spitoni et al. (2019) (8.2 Gyr versus 4.3 Gyr). The earlier accretion in the Spitoni et al. (2019) model results in a slight overestimation of the age of the low- $[\alpha/\text{Fe}]$  stars. Secondly, the model by Spitoni et al. (2019) considers continuous gas accretion during the second delayed accretion phase with an exponentially declining time-scale of 8 Gyr. The late-accretion model proposed here, instead, considers a short burst of star formation with a time-scale of  $\sim 0.7$  Gyr for this second accretion phase. This is required to match the age difference between the stars formed prior to and at the end of the late-accretion episode.

### 5.2.3 A heuristic scenario

Also in parallel to this work, Haywood et al. (2019) developed a heuristic scenario to explain the age–element abundance structure of the Galactic disc. In this scenario, the disc is pre-enriched by the formation of a high- $[\alpha/\text{Fe}]$  population (i.e. the chemical thick disc) and then diluted by metal-poor gas inflow from the outer disc that fuels a second phase of star formation and forms the

chemical thin disc. This model provides an interesting picture of the thick/thin disc formation but requires further refinements to match the detailed distribution of stars in the  $[\alpha/\text{Fe}]$ – $[\text{Fe}/\text{H}]$ –age space. For example, one of the challenges faced by this scenario is the observed coexistence of young, metal-poor and old, metal-rich populations in the low- $\alpha$  sequence.

### 5.2.4 Delayed accretion in cosmological models

It is interesting to note that delayed gas accretion has already been considered in hydrodynamical simulations (Birnboim, Dekel & Neistein 2007) and semi-analytic models (Calura & Menci 2009). In fact, the presence of a flat low- $\alpha$  sequence that resembles the now observed low- $\alpha$  sequence but with much lower  $[\alpha/\text{Fe}]$  was predicted in Calura & Menci (2009) thanks to the delayed gas accretion in their model.

## 6 SUMMARY

We investigate the age–element abundance structure of the Galactic outer disc ( $10 < r < 15$  kpc) as observed by the APOGEE survey. We construct a chemical evolution model and propose a new scenario for the chemical enrichment history of the outer disc to match the data. The key result is that our model invokes an additional recent gas accretion event.

We first examine the distribution of the outer disc stars in the  $[\alpha/\text{Fe}]$ – $[\text{Fe}/\text{H}]$  diagram. All stars follow an anticorrelation with decreasing  $[\alpha/\text{Fe}]$  with increasing  $[\text{Fe}/\text{H}]$ . With recently published age measurements for a large sample of stars observed by the APOGEE survey, we further utilize the distribution of stars in the three-dimensional space  $[\alpha/\text{Fe}]$ – $[\text{Fe}/\text{H}]$ –age to better constrain the chemical enrichment history of the outer disc. We identify two sequences of the  $[\alpha/\text{Fe}]$ – $[\text{Fe}/\text{H}]$  relation with different ages. Surprisingly, the younger stars with age  $< 6$  Gyr are less metal rich than the older stars.

This age–metallicity anticorrelation suggests a rather complicated chemical enrichment history. The young stars must have formed in a metal-poor environment that has been diluted by recent, metal-poor gas accretion. Equally surprising is that the first generation of stars that formed out of the diluted gas also has enhanced  $\alpha$ -abundances with  $[\alpha/\text{Fe}] \sim 0.14$  dex. This further implies that a starburst was triggered along with the gas accretion event boosting the  $\alpha$ -abundance through the enrichment from short-lived Type-II supernova. Moreover, the relatively low metallicities observed for this population suggest that the dilution has been very

effective. This in turn implies that a relatively large amount of metal-poor gas has been accreted. We estimate the mass of the accreted gas to be roughly three times the gas reservoir in the Galactic outer disc at the epoch of accretion.

We use a full chemical evolution model to constrain this late-accretion scenario. We explore traditional models assuming single exponentially declining gas accretion over cosmic time referred to as single- $\tau$  model as well as alternative models that include an additional short-term gas accretion event at a cosmic time of 8.2 Gyr ( $z \sim 0.6$ ) on top of the smooth, long-term accretion. The delay time is constrained by the age of the metal-rich stars in the low- $\alpha$  sequence. We call this alternative model ‘late-accretion model’. By comparing the prediction of these models with observations in the three-dimensional parameter space  $[\alpha/\text{Fe}]$ – $[\text{Fe}/\text{H}]$ –age, we find that the late-accretion model including a second accretion phase with a relatively short time-scale of  $\sim 0.7$  Gyr matched the data best.

We also investigate the potential effect of radial migration and find that radial migration helps to relieve the tension between the single- $\tau$  model and the observational data, but it is still not able to fully explain the observations. Our simulations suggest that the MW accreted roughly three times the gas reservoir of the outer disc at  $z \sim 0.6$  during this late-accretion episode. Our simulations further imply that a starburst was triggered during accretion. These characteristics imply that the late-accretion event may have been triggered by a galaxy merger event. If true, the data can be used to infer the properties of the accreted galaxy. The gas accretion from the infalling system must be lower than  $\sim -0.5$  dex, suggesting a dwarf galaxy with a stellar mass  $M_* < 10^9 M_\odot$  according to the mass–metallicity relation at intermediate redshift. Assuming the accreted gas distributed homogeneously within the outer disc, we estimate that the gas fraction of the accreted galaxy must have been  $\sim 75$  per cent. It will be interesting in future work to further explore the kinematic and dynamical effects of our late-accretion model on the evolution of the outer Galactic disc.

## ACKNOWLEDGEMENTS

We thank the anonymous referee for constructive comments and suggestions that significantly improved the clarity and robustness of the paper. JL is grateful to Gail Zasowski for help in the introduction of the APOGEE project and useful general comments and suggestions and Sten Hasselquist for useful discussions.

The Science, Technology and Facilities Council is acknowledged for support through the Consolidated Grant ‘Cosmology and Astrophysics at Portsmouth’, ST/N000668/1. Numerical computations were done on the Sciama High Performance Compute (HPC) cluster that is supported by the ICG, SEPnet, and the University of Portsmouth. OZ and DAGH acknowledge support from the State Research Agency (AEI) of the Spanish Ministry of Science, Innovation and Universities (MCIU) and the European Regional Development Fund (FEDER) under grant AYA2017-88254-P. JGF-T is supported by FONDECYT No. 3180210 and Becas Iberoamérica Investigador 2019, Banco Santander Chile.

Funding for the Sloan Digital Sky Survey IV has been provided by the Alfred P. Sloan Foundation, the U.S. Department of Energy Office of Science, and the Participating Institutions. SDSS acknowledges support and resources from the Center for High-Performance Computing at the University of Utah. The SDSS web site is [www.sdss.org](http://www.sdss.org).

SDSS is managed by the Astrophysical Research Consortium for the Participating Institutions of the SDSS Collaboration including the Brazilian Participation Group, the Carnegie Institution for

Science, Carnegie Mellon University, the Chilean Participation Group, the French Participation Group, Harvard-Smithsonian Center for Astrophysics, Instituto de Astrofísica de Canarias, The Johns Hopkins University, Kavli Institute for the Physics and Mathematics of the Universe (IPMU)/University of Tokyo, the Korean Participation Group, Lawrence Berkeley National Laboratory, Leibniz Institut für Astrophysik Potsdam (AIP), Max-Planck-Institut für Astronomie (MPIA Heidelberg), Max-Planck-Institut für Astrophysik (MPA Garching), Max-Planck-Institut für Extraterrestrische Physik (MPE), National Astronomical Observatories of China, New Mexico State University, New York University, University of Notre Dame, Observatório Nacional/MCTI, The Ohio State University, Pennsylvania State University, Shanghai Astronomical Observatory, United Kingdom Participation Group, Universidad Nacional Autónoma de México, University of Arizona, University of Colorado Boulder, University of Oxford, University of Portsmouth, University of Utah, University of Virginia, University of Washington, University of Wisconsin, Vanderbilt University, and Yale University.

## REFERENCES

- Abolfathi B. et al., 2018, *ApJS*, 235, 42  
 Adibekyan V. Z., Santos N. C., Sousa S. G., Israelian G., 2011, *A&A*, 535, L11  
 Adibekyan V. Z., Sousa S. G., Santos N. C., Delgado Mena E., González Hernández J. I., Israelian G., Mayor M., Khachatryan G., 2012, *A&A*, 545, A32  
 Alam S. et al., 2015, *ApJS*, 219, 12  
 Anders F. et al., 2017, *A&A*, 597, A30  
 Audouze J., Tinsley B. M., 1976, *ARA&A*, 14, 43  
 Bensby T., Feltzing S., Oey M. S., 2014, *A&A*, 562, A71  
 Bergemann M. et al., 2014, *A&A*, 565, A89  
 Birnboim Y., Dekel A., Neistein E., 2007, *MNRAS*, 380, 339  
 Bland-Hawthorn J., Gerhard O., 2016, *ARA&A*, 54, 529  
 Blanton M. R. et al., 2017, *AJ*, 154, 28  
 Borucki W. J. et al., 2010, *Science*, 327, 977  
 Bovy J., Rix H.-W., Hogg D. W., 2012, *ApJ*, 751, 131  
 Bovy J., Rix H.-W., Liu C., Hogg D. W., Beers T. C., Lee Y. S., 2012, *ApJ*, 753, 148  
 Bovy J., Rix H.-W., Schlafly E. F., Nidever D. L., Holtzman J. A., Shetrone M., Beers T. C., 2016, *ApJ*, 823, 30  
 Bressan A., Marigo P., Girardi L., Salasnich B., Dal Cero C., Rubele S., Nanni A., 2012, *MNRAS*, 427, 127  
 Calura F., Menci N., 2009, *MNRAS*, 400, 1347  
 Carraro G., Vázquez R. A., Costa E., Ahumada J. A., Giorgi E. E., 2015, *AJ*, 149, 12  
 Chiappini C., 2009, in Andersen J., Bland-Hawthorn J., Nordström B., eds, *Proc. IAU Symp. 254, The Galaxy Disc in Cosmological Context*. Kluwer, Dordrecht, p. 191  
 Chiappini C., Matteucci F., Gratton R., 1997, *ApJ*, 477, 765  
 Chiappini C., Matteucci F., Romano D., 2001, *ApJ*, 554, 1044  
 Chiappini C. et al., 2015, *A&A*, 576, L12  
 Clarke A. J. et al., 2019, *MNRAS*, 484, 3476  
 Colina L., Arribas S., Monreal-Ibero A., 2005, *ApJ*, 621, 725  
 De Silva G. M. et al., 2015, *MNRAS*, 449, 2604  
 Einasto J., 1979, in Burton W. B., ed., *Proc. IAU Symp. 84, The Large-Scale Characteristics of the Galaxy*. D. Reidel Publ. Co., Dordrecht, p. 451  
 Feuillet D. K. et al., 2018, *MNRAS*, 477, 2326  
 Fuhrmann K., 1998, *A&A*, 338, 161  
 García Pérez A. E. et al., 2016, *AJ*, 151, 144  
 Gibbons S. L. J., Belokurov V., Evans N. W., 2017, *MNRAS*, 464, 794  
 Grand R. J. J. et al., 2017, *MNRAS*, 467, 179  
 Greggio L., Renzini A., 1983, *A&A*, 118, 217  
 Gunn J. E. et al., 2006, *AJ*, 131, 2332  
 Hayden M. R. et al., 2015, *ApJ*, 808, 132

- Haywood M., Di Matteo P., Lehnert M. D., Katz D., Gómez A., 2013, *A&A*, 560, A109
- Haywood M., Snaith O. N., Lehnert M. D., Di Matteo P., Khoperskov S., 2019, *A&A*, 625, A105
- Helmi A., Babusiaux C., Koppelman H. H., Massari D., Veljanoski J., Brown A. G. A., 2018, *Nature*, 563, 85
- Holtzman J. A. et al., 2015, *AJ*, 150, 148
- Holtzman J. A. et al., 2018, *AJ*, 156, 125
- Ibata R. A., Gilmore G., Irwin M. J., 1994, *Nature*, 370, 194
- Jørgensen B. R., Lindegren L., 2005, *A&A*, 436, 127
- Kalberla P. M. W., Kerp J., Dedes L., Haud U., 2014, *ApJ*, 794, 90
- Kennicutt R. C., Jr, 1998, *ARA&A*, 36, 189
- Kennicutt R. C., Jr et al., 2007, *ApJ*, 671, 333
- Kobayashi C., Umeda H., Nomoto K., Tominaga N., Ohkubo T., 2006, *ApJ*, 653, 1145
- Kroupa P., 2001, *MNRAS*, 322, 231
- Leroy A. K., Walter F., Brinks E., Bigiel F., de Blok W. J. G., Madore B., Thornley M. D., 2008, *AJ*, 136, 2782
- Lian J. et al., 2019, *MNRAS*, 489, 1436
- Lian J., Hu N., Fang G., Ye C., Kong X., 2016, *ApJ*, 819, 73
- Lian J., Thomas D., Maraston C., Goddard D., Comparat J., Gonzalez-Perez V., Ventura P., 2018a, *MNRAS*, 474, 1143
- Lian J. et al., 2018b, *MNRAS*, 476, 3883
- Lian J., Thomas D., Maraston C., 2018c, *MNRAS*, 481, 4000
- Lilly S. J., Carollo C. M., Pipino A., Renzini A., Peng Y., 2013, *ApJ*, 772, 119
- Ma X., Hopkins P. F., Wetzel A. R., Kirby E. N., Anglés-Alcázar D., Faucher-Giguère C.-A., Kereš D., Quataert E., 2017, *MNRAS*, 467, 2430
- Mackereth J. T. et al., 2017, *MNRAS*, 471, 3057
- Mackereth J. T., Crain R. A., Schiavon R. P., Schaye J., Theuns T., Schaller M., 2018, *MNRAS*, 477, 5072
- Maiolino R., Mannucci F., 2019, *A&AR*, 27, 3
- Majewski S. R. et al., 2017, *AJ*, 154, 94
- Maoz D., Mannucci F., Brandt T. D., 2012, *MNRAS*, 426, 3282
- Martig M. et al., 2015, *MNRAS*, 451, 2230
- Matteucci F., 1994, *A&A*, 288, 57
- Matteucci F., Greggio L., 1986, *A&A*, 154, 279
- Matteucci F., Panagia N., Pipino A., Mannucci F., Recchi S., Della Valle M., 2006, *MNRAS*, 372, 265
- McKee C. F., Parravano A., Hollenbach D. J., 2015, *ApJ*, 814, 13
- McMillan P. J., 2011, *MNRAS*, 414, 2446
- Mihos J. C., Bothun G. D., 1998, *ApJ*, 500, 619
- Minchev I., Chiappini C., Martig M., 2013, *A&A*, 558, A9
- Ness M., Hogg D. W., Rix H.-W., Martig M., Pinsonneault M. H., Ho A. Y. Q., 2016, *ApJ*, 823, 114
- Nidever D. L. et al., 2015, *AJ*, 150, 173
- Noguchi M., 2018, *Nature*, 559, 585
- Pagal B. E. J., 1997, in Pagal B. E. J., ed., *Nucleosynthesis and Chemical Evolution of Galaxies* (ISBN 0521550610). Cambridge Univ. Press, Cambridge, UK, p. 392
- Pagal B. E. J., Patchett B. E., 1975, *MNRAS*, 172, 13
- Pinsonneault M. H. et al., 2014, *ApJS*, 215, 19
- Pinsonneault M. H. et al., 2018, *ApJS*, 239, 32
- Reddy B. E., Lambert D. L., Allende Prieto C., 2006, *MNRAS*, 367, 1329
- Robin A. C., Reylé C., Derrière S., Picaud S., 2003, *A&A*, 409, 523
- Robin A. C., Marshall D. J., Schultheis M., Reylé C., 2012, *A&A*, 538, A106
- Savaglio S. et al., 2005, *ApJ*, 635, 260
- Schmidt M., 1963, *ApJ*, 137, 758
- Schönrich R., Binney J., 2009, *MNRAS*, 396, 203
- Spitoni E., Silva Aguirre V., Matteucci F., Calura F., Grisoni V., 2019, *A&A*, 623, A60
- Strolger L.-G. et al., 2004, *ApJ*, 613, 200
- Tepper-García T., Bland-Hawthorn J., 2018, *MNRAS*, 478, 5263
- Thomas D., Greggio L., Bender R., 1998, *MNRAS*, 296, 119
- Thomas D., Maraston C., Schawinski K., Sarzi M., Silk J., 2010, *MNRAS*, 404, 1775
- Tumlinson J., 2010, *ApJ*, 708, 1398
- van den Bergh S., 1962, *AJ*, 67, 486
- Wilson J. C. et al., 2012, in Ian S. M., Suzanne K. R., Hideki T., eds, *Proc. SPIE Conf. Ser. Vol. 8446, Ground-Based and Airborne Instrumentation for Astronomy IV*. SPIE, Bellingham, p. 84460H
- Wilson J. C. et al., 2019, *PASP*, 131, 055001
- Wolfire M. G., McKee C. F., Hollenbach D., Tielens A. G. G. M., 2003, *ApJ*, 587, 278
- Wu Y. et al., 2018, *MNRAS*, 475, 3633
- Wu Y. et al., 2019, *MNRAS*, 484, 5315
- Zasowski G. et al., 2013, *AJ*, 146, 81
- Zasowski G. et al., 2017, *AJ*, 154, 198
- Zhang C. et al., 2019, *ApJ*, 884, L52
- Zhao G., Zhao Y., Chu Y., Jing Y., Deng L., 2012, preprint ([arXiv:1206.3569](https://arxiv.org/abs/1206.3569))

This paper has been typeset from a  $\text{\TeX}/\text{\LaTeX}$  file prepared by the author.